Ultramicroscopy 159 (2015) 101–111

Contents lists available at ScienceDirect

Ultramicroscopy

journal homepage: www.elsevier.com/locate/ultramic

Effects of detector dead-time on quantitative analyses involving boron and multi-hit detection events in atom probe tomography

Frederick Meisenkothen [a,*], Eric B. Steel [a], Ty J. Prosa [b], Karen T. Henry [c], R. Prakash Kolli [d]

[a] Materials Measurement Science Division, National Institute of Standards and Technology, Gaithersburg, MD 20899, USA
[b] CAMECA Instruments, Inc., 5500 Nobel Drive, Madison, WI 53711, USA
[c] Intel Corporation, Hillsboro, OR, 97124, USA
[d] Department of Materials Science and Engineering, 2144 Chemical and Nuclear Engineering, Building #090, University of Maryland, College Park, MD 20742, USA

ARTICLE INFO

Article history:
Received 24 February 2015
Received in revised form
7 July 2015
Accepted 26 July 2015
Available online 29 July 2015

Keywords:
Atom probe
Dead-time
Boron
Dopant
Multi-hit
Field evaporation

ABSTRACT

In atom probe tomography (APT), some elements tend to field evaporate preferentially in multi-hit detection events. Boron (B) is one such element. It is thought that a large fraction of the B signal may be lost during data acquisition and is not reported in the mass spectrum or in the 3-D APT reconstruction. Understanding the relationship between the field evaporation behavior of B and the limitations for detecting multi-hit events can provide insight into the signal loss mechanism for B and may suggest ways to improve B detection accuracy. The present work reports data for nominally pure B and for B-implanted silicon (Si) (NIST-SRM2137) at dose levels two-orders of magnitude lower than previously studied by Da Costa, et al. in 2012. Boron concentration profiles collected from SRM2137 specimens qualitatively confirmed a signal loss mechanism is at work in laser pulsed atom probe measurements of B in Si. Ion correlation analysis was used to graphically demonstrate that the detector dead-time results in few same isotope, same charge-state (SISCS) ion pairs being properly recorded in the multi-hit data, explaining why B is consistently under-represented in quantitative analyses. Given the important role of detector dead-time as a signal loss mechanism, the results from three different methods of estimating the detector dead-time are presented. The findings of this study apply to all quantitative analyses that involve multi-hit data, but the dead-time will have the greatest effect on the elements that have a significant quantity of ions detected in multi-hit events.

Published by Elsevier B.V.

1. Introduction

The International Technology Roadmap for Semiconductors (ITRS) has repeatedly listed accurate dopant profiling among the technical requirements needed for modeling inputs and for the creation of reference materials [1,2]. Additionally, the roadmap states that "materials characterization … methods are needed for control of … dopant positions, … and atomic concentrations relative to device dimensions". Atom probe tomography (APT) has the required sub-nanometer spatial resolution (<0.2 nm lateral and <0.1 nm along the analysis direction) [3] and high elemental sensitivity (atom fraction less than 10^{-5}) to meet these characterization needs [4,5]. Moreover, the APT detection system can detect all elements in the periodic table, and the elements can be detected without prior knowledge of the specimen composition [5,6]. Site specific specimen extraction via dual-beam focused ion beam/scanning electron microscope (FIB/SEM) instruments has facilitated the use of APT for semiconductor device analysis [4,5,7]. It has been demonstrated that APT can be used to measure dopant profiles accurately in silicon (Si) with careful specimen preparation and data acquisition techniques [8,9]. However, some elements, such as boron (B), tend to field evaporate preferentially in multi-hit detection events, during APT [10–12]. The limited ability of the atom probe detector to resolve multi-hit events, also known as ion pile-up, has been identified as a mechanism through which preferential loss of signal for an elemental species can occur, thereby causing inaccurate measurement of concentration and isotopic abundance [13–18,56]. Boron is an important p-type dopant used in the fabrication of microelectronic devices. Additionally, B has been implicated in the formation of nano-scale defects, known as boron interstitial clusters (BICs), in device structures. The BICs may contain only a few atoms, but large defects contain hundreds of atoms [19,20]. A large amount of the total B signal may be lost during atom probe data acquisition [5,10] making it difficult to determine the local B dopant concentration and to detect BICs.

* Correspondence to: National Institute of Standards and Technology, 100 Bureau Drive, MS-8372, Gaithersburg, MD 20899 U.S.A.
E-mail address: frederick.meisenkothen@nist.gov (F. Meisenkothen).

http://dx.doi.org/10.1016/j.ultramic.2015.07.009
0304-3991/Published by Elsevier B.V.

An increased understanding of the field evaporation behavior of elements that are preferentially detected in multi-hit events, such as B, can lead to improved measurement accuracy for semiconductor dopants, isotopic abundances, and quantitative analyses in multi-component materials. Thus, the focus of this article is a study of the field evaporation behavior of high and minor-to-trace concentrations of B in multi-hit events during pulsed-laser APT. The work expands the range of study beyond that which had been previously reported for high doses of B-implanted in Si (1×10^{17} atoms cm^{-2}) [10]. The field evaporation behavior of nominally pure B, and B-implanted Si (1×10^{15} atoms cm^{-2}) was studied using a state-of-the-art atom probe instrument with an ultraviolet (UV) pulsed-laser and a three-anode delay line detector (DLD) in the standard configuration. The differences in mass spectra for nominally pure B and ^{10}B-implanted Si are discussed in regards to apparent isotopic abundances. Ion correlation analyses are presented to graphically demonstrate the effects of multiple ion field evaporation. An analytical solution is provided for the depleted data zone boundary on the ion correlation histogram, and is used to estimate the detector dead-time. The detector dead-time is also estimated by a TOF-based ion correlation analysis and a TOF filter method. The multi-hit event behavior of arsenic-implanted Si was analyzed with an earlier generation atom probe instrument that has a known dead-time in order to confirm the dead-time analyses. The magnitude of the B signal loss is discussed. Additionally, the effects of ion pile-up on the isotopic abundances of Si are included to demonstrate the important point that the dead-time affects all elements in the multi-hit detection events.

1.1. Multi-hit events

A multi-hit event is defined as a detection event in which more than one ion is detected in association with a given laser pulse (or voltage pulse). Multi-hit events, also referred to as multiples, are denoted by an event multiplicity that specifies the number of constituent ions within the detection event, e.g. multiplicity-2 [15,21]. The physical mechanism for field evaporation of multiple ions has been attributed to chemical and geometrical effects that include differences in the local bonding environment for atoms on the specimen surface and the different evaporation fields that are required to ionize the constituent atomic species [13,15,22,23].

During pulsed-laser or pulsed-voltage APT, the field evaporated ions travel to a position sensitive detector that records the positions of the incident ions in the x–y plane [24–26]. State-of-the-art detectors in commercial CAMECA[1] local-electrode atom probe (LEAP®) instruments employ micro-channel plates (MCPs) in front of crossed helical or serpentine DLDs in order to detect the incident ions. The z-position is determined from the field evaporation sequence of each ion, and the mass-to-charge-state ratio (m/n) is determined from the time-of-flight (TOF) [27–30].

The crossed helical or serpentine DLDs that are used for ion detection have a limited ability to resolve multi-hit events. When multiple ions impact the detector between successive pulses, the constituent ions of the multi-hit event need to be properly identified through the timing signals that were recorded by the DLD anodes. The signal pulses, each typically < 5 ns in duration [31], are created by the electron cloud cascade that is generated by an ion impact on the MCP. A typical DLD system has an electronic dead-time that is between 5 and 20 ns depending on the design [32–34]. During this dead-time, multiple ion impacts on the detector cannot be differentiated from one another, i.e. the system perceives the multi-hit event as a single-hit event. The effect is also referred to as ion pile-up [16–18,35,36]. However, if the constituent ions in the multi-hit event arrive sufficiently far apart on the detector, the spatial difference can permit the individual ions of the multi-hit event to be resolved even if the ions have the same TOF. The dead-time thus corresponds to a physical dead-zone that surrounds each ion impact site, where a second ion cannot be detected if it arrives within a specified time interval [34].

Recent studies on the behavior of the ions that comprise multi-hit events indicate that they are closely correlated in space and time [15,22,37,38], while ions uncorrelated with the pulse tend to be single-hit events that contribute to the background noise signal [15,38]. Hence, filtering techniques can be used to extract the ion information for the high-multiplicity events, and thereby provide a mass spectrum that has an improved signal-to-noise ratio [15]. Furthermore, since some elements are more prone to field evaporate in multi-hit events [9,11–15], a similar filtering scheme can be used to enhance detection sensitivity for these elements. Atomic species that are prone to field evaporate in multi-hit events are susceptible to a preferential signal loss due to the aforementioned detector dead-time and the DLD dead-zone. The effect of signal loss for a particular species is loss of accuracy in measured elemental concentrations and isotopic abundances [13–18].

2. Experimental

2.1. Materials

Two different specimen materials containing B were used in this study. One of the materials, nominally pure B, was chosen to represent a very high concentration of B. The second material was the National Institute of Standards and Technology (NIST) Standard Reference Material (SRM) 2137 (B implanted in Si), which was developed as a calibration standard for minor and trace concentrations of B in a Si matrix during secondary ion mass spectrometry (SIMS) [39,40]. The SRM2137 wafer substrate consists of a single crystal of [100] oriented n-type Si. The wafer was implanted with ^{28}Si at the surface in order to make this region appear amorphous to the ^{10}B ion beam that was later used to implant the B. The retained dose of ^{10}B is about 1×10^{15} atoms cm^{-2} and the depth profile has a peak concentration at about 188 nm below the surface. In order to preserve the implant zone during the APT specimen preparations, the SRM2137 material was coated with < 100 nm thick layer of sputter deposited Si in a SBT[1] IBS/e system prior to ion milling in the dual-beam FIB/SEM instrument. Three Si pre-sharp specimens (commercially available from CAMECA) were also used in this study, as well as a B-doped Si nanowire (SiNW) that was grown at NIST via chemical vapor deposition (CVD). The data from the SiNW specimen was used solely to map the detector dead-zone.

Additionally, an arsenic-implanted Si wafer was used in this study to provide a comparative reference with an earlier generation atom probe instrument, as described below. The wafer was implanted with arsenic (As) at 50 keV with a dose of 2×10^{15} atoms cm^{-2}. The wafer was subsequently capped with CVD poly-Si, annealed at 600 °C, and then spike annealed at 1000 °C. A < 100 nm thick layer of nickel (Ni) was deposited on the surface in an SBT IBS/e system prior to ion milling in the dual-beam FIB/SEM instrument.

[1] Disclaimer

Certain commercial equipment, instruments, or materials are identified in this paper in order to specify the experimental procedure adequately. Such identification is not intended to imply recommendation or endorsement by the National Institute of Standards and Technology, nor is it intended to imply that the materials or equipment identified are necessarily the best available for the purpose.

2.2. APT specimen preparation

The B and SRM2137 APT specimens were prepared with a FEI Nova 600 dual-beam FIB/SEM instrument. An *in-situ* lift-out technique was employed to remove a rectangular wedge of specimen material for placement on Si micro-tip post arrays [7,41] that are available from CAMECA. An annular milling procedure that minimizes gallium (Ga) ion implantation was followed [42]. The ion beam was then set to 5 keV and 28 pA and allowed to raster over the specimen and surrounding areas for ≈ 10 s to remove material that had been damaged by the 30 keV Ga ion beam annular milling operation [43]. The arsenic-implanted Si specimen was also prepared using a similar conventional *in-situ* lift-out technique and annular milling procedure in a dual-beam FIB/SEM instrument. The three Si pre-sharp specimens did not require any specimen preparation prior to analysis. The SiNW specimen was lifted from the growth substrate and transferred to a Si micro-tip post via *in-situ* lift-out in the dual-beam FIB/SEM instrument using only the electron beam for imaging and platinum (Pt) deposition.

2.3. Atom probe tomography instruments

A CAMECA LEAP® 4000X-Si/HR instrument was employed to acquire the data for all of the specimens except the arsenic-implanted Si. The specimen acquisition conditions are provided in Table 1. The flight path length for the HR configuration is fixed at approximately 382 mm. A flight path length of 90 mm was used for the Si configuration. The instrument is equipped with a 355 nm wavelength UV pulsed-laser. The laser polarization direction was chosen to be parallel to the specimen axis in an effort to maximize the efficiency with which the specimen is heated [44]. The data acquired with the HR instrument configuration was used solely to demonstrate qualitatively that a loss of the B signal occurs in the LEAP® 4000X-HR configuration as well as the LEAP® 4000X-Si configuration. The active area of the MCP in the LEAP® 4000X-Si instrument is nominally 75 mm, whereas that for the LEAP® 4000X-HR is nominally 37 mm. The LEAP® 4000X uses a three anode DLD.

A pre-2006 model year LEAP® 3000X-Si instrument with a straight flight path of 84 mm was employed for data acquisition of the arsenic-implanted Si specimen. The instrument is equipped with a 532 nm wavelength green pulsed-laser. The significance of the data from this instrument lies in the fact that it used an earlier style DLD system with two anodes and a known dead-time of approximately 18 ns–20 ns permitting comparison with the state-of-the art atom probe instruments and verification of the dead-time estimations. The active area of the MCP in the LEAP® 3000X-Si instrument is nominally 75 mm.

2.4. APT data reconstruction and analysis

The reconstruction and data analysis were performed with the CAMECA Integrated Visualization and Analysis Software (IVAS®), version 3.6.6 following standard procedures [27–29,45]. After the reconstruction was completed, the mass spectrum for each dataset was partitioned into three subset mass spectra; one that contained only single hit events, one that contained only multi-hit events, and one that contained both single and multi-hit events. A linear fit to the background was used to estimate and remove the background signal from the mass spectra. Two ion ranges near to, but not including, the B peaks were defined and used to estimate the average background counts per channel that would define the linear fit under the peak.

The individual ion information from the dataset was exported to a binary ∗.ePOS data file in order to analyze the data. Details of the information contained in the ∗.ePOS file can be found in the following references [46,47]. A custom algorithm was used to read and filter the ion data in the ∗.ePOS data files. The algorithm is designed to search, sort, and extract specific ion data, based on a defined set of criteria. The extracted ion information was used to study the relationships between the individual ions in the multi-hit events and to plot mass spectra, multiplicity frequency distributions, and ion correlation histograms. The ion correlation analyses graphically demonstrate relationships between the constituent ions of each multi-hit event and provides insight into the field evaporation behavior of a material under a given set of acquisition conditions [33,48]. In this study, the (m/n) ratio or TOF from the first ion in the multi-hit event (also denoted first-of-multiples) was plotted versus the (m/n) ratio or TOF from the second ion in the multi-hit event (also denoted second-of-multiples). The resulting two-dimensional (2-D) ion correlation histograms provide a means for detecting and identifying complex ions, molecular ions, and neutral species through ion dissociation reactions that appear as curved tracks in the histogram [48,49]. The histograms also indicate sympathetic or co-evaporation events, where one specific type of ion consistently and simultaneously field evaporates with another specific type of ion. The co-evaporation events include the coincidence points, which are points generated by the ions comprising the major (m/n) ratio peaks in the mass spectrum, and also provide a method for identifying the ions that comprise the corresponding peak tails [48].

3. Results and discussion

3.1. Boron depth profiles – confirmation of signal loss

Fig. 1 provides a comparison of the ^{10}B concentration depth profile, as measured by SIMS and reported in the NIST SRM2137

Table 1
Ion counts, by isotope and charge-state, for nominally pure boron.

Material	Instrument	Flight path (mm)	Temperature (K)	Laser pulse energy (pJ)	Pulse frequency (kHz)	Detection rate (%)	Chamber pressure (Pa)
B	LEAP 4000X-Si	90	40	20	500	0.2	1.2×10^{-8}
B	LEAP 4000X-Si	90	40	30	500	0.2	1.2×10^{-8}
Si	LEAP 4000X-Si	90	40	1,2,4,8,16,32	500	0.5	1.3×10^{-8}
Si	LEAP 4000X-Si	90	40	64	500	0.5	1.3×10^{-8}
Si	LEAP 4000X-Si	90	40	Voltage pulsed (15%PF)	200	1	1.2×10^{-8}
Si(B)-NW	LEAP 4000X-Si	90	40	20	500	1	6.7×10^{-8}
SRM2137	LEAP 4000X-Si	90	40	20	500	0.2	1.2×10^{-8}
SRM2137	LEAP 4000X-HR	382	30	35	250	1	6.7×10^{-8}
Si(As)	LEAP 3000X-Si[a]	84	30	1000	250	0.5	6.7×10^{-8}

[a] The LEAP 3000X-Si instrument uses a 532 nm wavelength green laser.

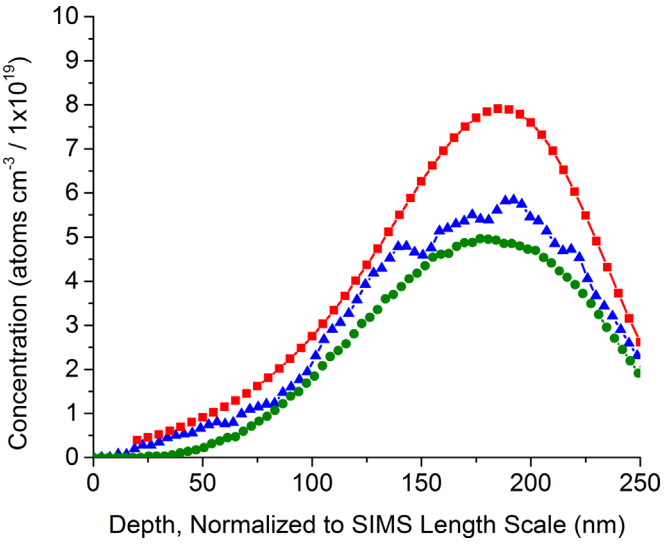

Fig. 1. Concentration depth profiles for ^{10}B in SRM2137 (smoothed by adjacent point averaging). The red squares indicate the SIMS data listed in the SRM certificate. The blue triangles (4000X-Si) and green circles (4000X-HR) indicate the APT data. (For interpretation of the references to color in this figure legend, the reader is referred to the web version of this article.)

certificate [39], with the ^{10}B concentration depth profiles, as measured by APT. Since the implant zone was amorphized, no crystallographic features are available in the APT data set for use as an internal length scale calibration [8] for the 3-D reconstruction parameters. The APT data length scales have been normalized to the SIMS data length scale in order to bring the peak centroids of the three data sets into alignment with one another. The integrated areas under the curves indicate that approximately 23% (Si configuration) to 36% (HR configuration) of the B signal has been lost in the APT data, relative to the SIMS data, thereby verifying a loss mechanism is at work.

3.2. Mass spectra

Sections of the mass spectra for the nominally pure B specimens are illustrated in Fig. 2(a)–(b). The (m/n) ratios for the multi-hit mass spectra have been shifted to the right by 0.1 Da in the figures to make it easier to distinguish between the single-hit (red filled trace) and the multi-hit (blue trace) spectra. Boron has two naturally occurring isotopes, ^{10}B and ^{11}B, with nominal fractional isotopic abundances of 0.199 and 0.801, respectively, although there is some natural isotopic variation. At a specific charge-state, the expected ratio of the natural isotopic abundances in the mass spectrum is 0.248. Table 2 lists, by isotope and charge-state, the background corrected counts for each major peak in the nominally pure B mass spectra. The square root of the counted number was used as a measure of uncertainty. The ratio of the ^{10}B peak counts to the ^{11}B peak counts indicates that the reported isotope abundances in the multi-hit data are markedly different between the $1+$ and $2+$ charge-states. The measured isotopic abundance ratio for the $1+$ charge-state in the multi-hit spectra are 0.52 ± 0.03 for the 30 pJ acquisition and 0.51 ± 0.01 for the 20 pJ acquisition, both of which are greater than the naturally occurring ratio. The measured isotopic abundance ratios for the $2+$ charge-state are 0.36 ± 0.02 for the 30 pJ acquisition and 0.39 ± 0.01 for the 20 pJ acquisition, both of which are also greater than the naturally occurring ratio. The relative error was defined as the measured ^{10}B to ^{11}B count ratio divided by the naturally occurring ^{10}B to ^{11}B abundance ratio. The ^{10}B to ^{11}B count ratios indicate that the major isotope, ^{11}B, is consistently under-represented, relative to the minor isotope, ^{10}B. A suppression of the reported major isotope

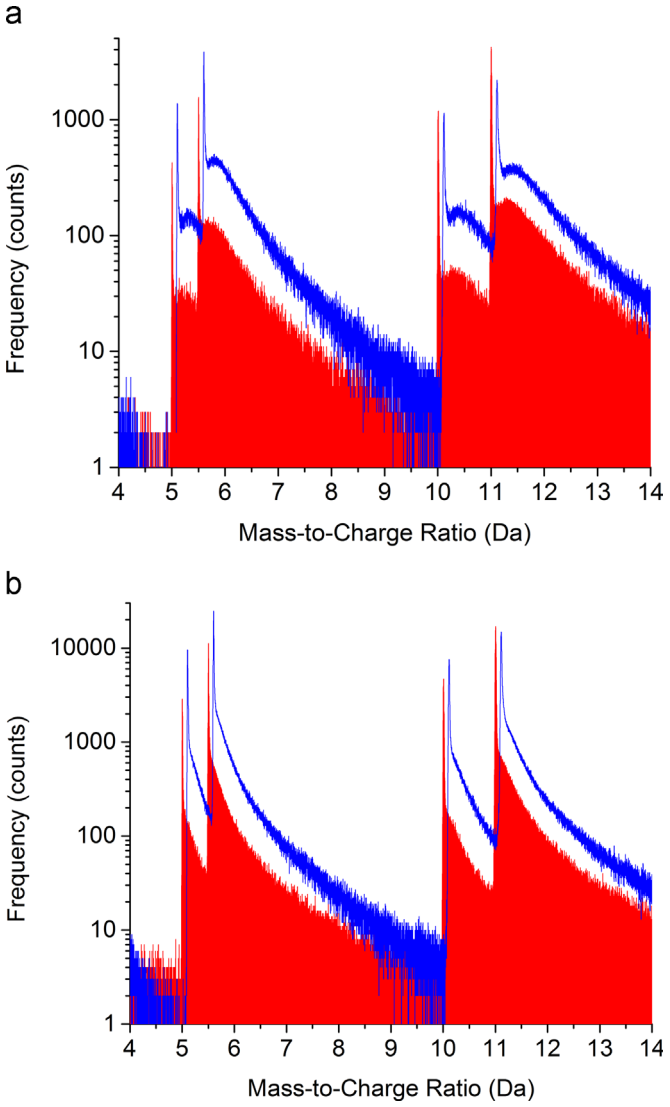

Fig. 2. Mass spectra sections for nominally pure B analyzed at a laser pulse energy of (a) 30 pJ and (b) 20 pJ. The red filled trace indicates the single detection events, while the blue unfilled trace indicates the multi-hit detection events. The (m/n) ratios for the multi-hit mass spectra have been shifted to the right by 0.1 Da for clarity. (For interpretation of the references to color in this figure legend, the reader is referred to the web version of this article.)

abundance has been previously reported for Fe and C [18], and for B in metallic glasses [50] in connection with ion pile-up related signal loss. The same trend is observed here in the single-hit mass spectra, but to a lesser extent, for reasons that are not yet understood. Fig. 2(a) and (b) demonstrate that the tail can have a different shape between two data sets indicating that the acquisition conditions influence the shape of the tails. The exact shapes that define the peak and tails in the mass spectra are unknown and complex in nature. The number of ions detected for the ^{11}B peak is over-counted due to the influence of ions from the ^{10}B tail, and thus the ^{10}B to ^{11}B count ratio should be higher than is reported in Table 2. No B hydride complex ion peak, i.e. ^{11}B^{1}H, was observed in the mass spectrum, indicating that there should be no ^{10}B^{1}H contribution to the ^{11}B peak. Table 2 also indicates that the number of higher charge-state ions is greater in the multi-hit spectra than in the single hit spectra, which is clearly visible in Fig. 2 (a) and (b), and is expected [12]. The mass spectra also contain other isotopic abundance anomalies. For example, in Fig. 2(a), the ^{10}B^{1+} peak of the single-hit and the multi-hit spectra have approximately the same number of counts. The expectation is that

Table 2
Ion counts, by isotope and charge-state, for nominally pure boron.

Ions	Singles (30 pJ) (counts)	Multi-hit (30 pJ) (counts)	All hits (30 pJ) (counts)	Singles (20 pJ) (counts)	Multi-hit (20 pJ) (counts)	All hits (20 pJ) (counts)
$^{10}B^{1+}$	1186 ± 34	1144 ± 34	2138 ± 46	4685 ± 68	7565 ± 87	11421 ± 107
$^{11}B^{1+}$	4227 ± 65	2200 ± 47	5770 ± 76	17041 ± 131	14896 ± 122	29280 ± 171
$^{10}B/^{11}B$ ratio	0.28 ± 0.01	0.52 ± 0.03	0.37 ± 0.01	0.27 ± 0.01	0.51 ± 0.01	0.39 ± 0.01
Rel. error (%)	12	108	48	10	103	56
$^{10}B^{2+}$	426 ± 21	1384 ± 37	1776 ± 42	2860 ± 53	9588 ± 98	12448 ± 112
$^{11}B^{2+}$	1561 ± 40	3826 ± 62	5334 ± 73	11203 ± 106	24901 ± 158	35649 ± 189
$^{10}B/^{11}B$ ratio	0.27 ± 0.02	0.36 ± 0.02	0.33 ± 0.01	0.26 ± 0.01	0.39 ± 0.01	0.35 ± 0.01
Rel. error (%)	9	45	33	2	54	40

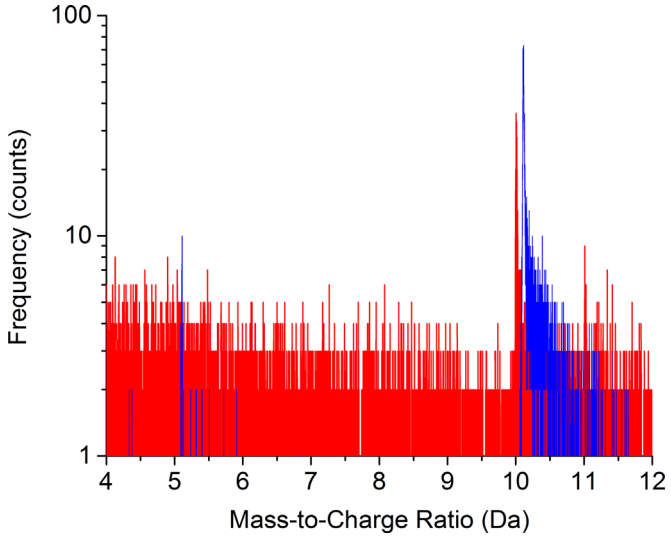

Fig. 3. Mass spectra sections for SRM2137 acquired on the 4000X-Si instrument at 20 pJ for single-hit (red filled trace) and multi-hit (blue trace) events. The (*m*/*n*) ratios for the multi-hit mass spectra have been shifted to the right by 0.1 Da for clarity. (For interpretation of the references to color in this figure legend, the reader is referred to the web version of this article.)

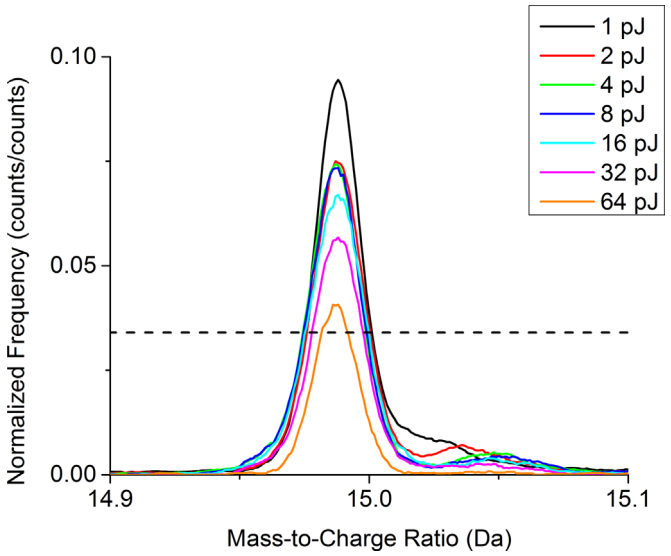

Fig. 4. Multiples-only mass spectra for Si pre-sharp specimens. The vertical axis has been normalized to the height of the $^{28}Si^{2+}$ peak to show that the reported isotopic abundance, indicated by the relative height of the $^{30}Si^{2+}$ peak, varies with acquisition conditions. The height ratio between the $^{30}Si^{2+}$ peak and the $^{28}Si^{2+}$ peak should be about 0.034 as indicated by the horizontal black dotted line. Generally, the number of multi-hit events decreases as the laser pulse energy is increased on the Si. (For color interpretation of this figure, the reader is referred to the web version of this article.)

the $^{11}B^{1+}$ peak maxima in both spectra should also be approximately equal in counts. However, the single-hit $^{11}B^{1+}$ peak has almost twice as many counts as the corresponding peak in the multi-hit spectrum. As a second example, the $^{11}B^{1+}$ peak maximum in the single-hit spectrum of Fig. 2(b) has more counts than the corresponding peak in the multi-hit spectrum. Therefore, one would expect that the $^{10}B^{1+}$ peak in the single-hit spectrum will have more counts than the corresponding peak in the multi-hit spectrum. However, Fig. 2(b) shows that the opposite is true.

Mass spectra sections for the SRM2137 specimen are provided in Fig. 3. The (*m*/*n*) ratios for the multi-hit mass spectrum have been shifted to the right by 0.1 Da in the figure to make it easier to distinguish between the single-hit (red filled trace) and the multi-hit (blue trace) spectra. As with the nominally pure B specimens, the 2+ charge state is preferentially detected in the multi-hit spectrum. Since the SRM2137 material is implanted with ^{10}B, a discussion of isotopic abundance would not be meaningful for this specimen.

Similar isotope ratio measurement bias can be observed for the other elements that are detected in the multi-hit events. The multiples-only mass spectra for two Si pre-sharp specimens are shown in Fig. 4. The number of counts in each bin on the mass spectrum has been normalized to the peak height intensity of the $^{28}Si^{2+}$ peak to show that the reported isotopic abundance, indicated by the relative height of the $^{30}Si^{2+}$ peak, varies with acquisition conditions. The height ratio between the $^{30}Si^{2+}$ peak and the $^{28}Si^{2+}$ peak should be about 0.034 for natural isotopic abundance, as indicated on Fig. 4 (black dotted horizontal line). Generally, for the Si data sets, the number of multi-hit events decreased as the laser pulse energy used during acquisition was increased. For example, approximately 11% of the detection events were multi-hit events at 1 pJ; however, only about 3.5% of the detection events were reported as multi-hit events at 64 pJ. A similar relationship between increased laser pulse energy and decreased multi-hit detection events has been reported in a study on Ti–Si–N [21]. As with the nominally pure B specimens, the isotope abundance in the multiples-only mass spectrum indicates that the major isotope, ^{28}Si, is under-represented. In this case, the peak-to-background ratios were in excess of 50 prior to normalization, and the tails from adjacent peaks do not add a significant contribution to the peak intensity. Further, any contributions to the peak intensities from Si hydride complex ions were insignificant. No discernable Si hydride complex ion peaks were observed in the mass spectra, e.g. at 15.5 Da or at 31 Da, and the sum of the hydrogen signals at 1 Da and 2 Da was found to increase as the laser pulse energy was increased from 1 pJ to 32 pJ on the one specimen. Therefore, the effects of DC field evaporation, noise, changing tail shapes, and Si hydride complex ions do not make a significant contribution to the relative isotopic abundances shown in Fig. 4, while the number of multi-hit events is correlated to the observed trend with laser pulse energy. Therefore, since the apparent

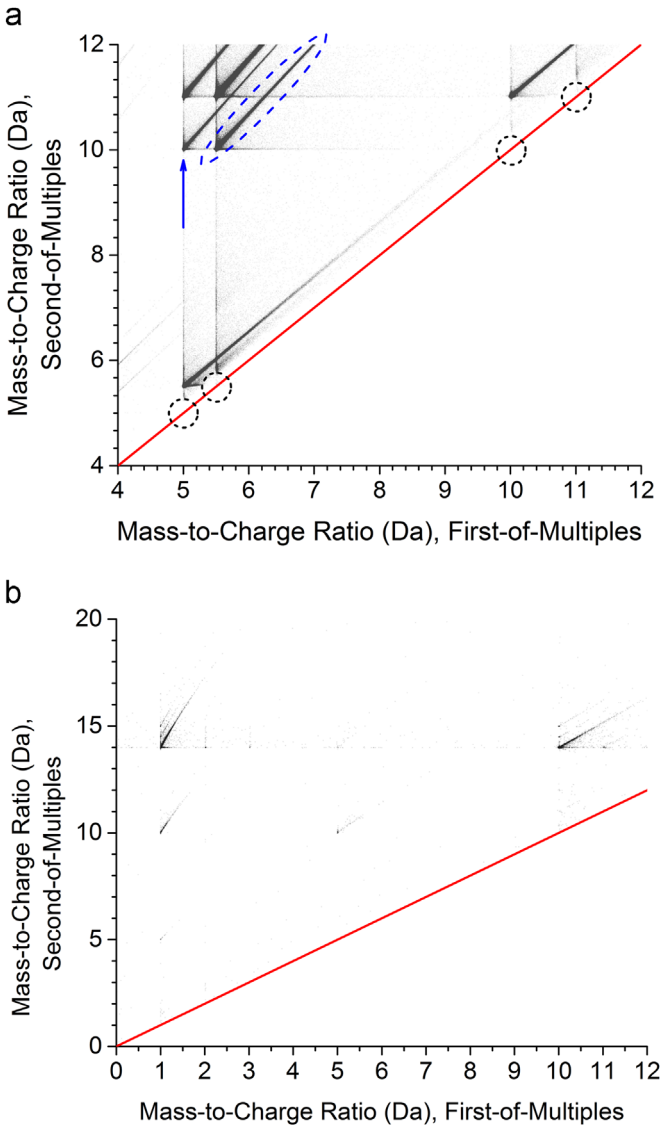

Fig. 5. Mass-to-charge ratio ion correlation histograms for (a) nominally pure B (20 pJ) and (b) SRM2137 (LEAP® 4000X-Si instrument) APT specimens. The diagonal red reference line indicates $y=x$. A depleted data zone is present adjacent to the $y=x$ line. In (a), SISCS ion pairs that are absent are indicated by dotted circles and a delayed evaporation track is indicated by the blue dashed oval on the plot. The arrow shows a coincidence point related to the $^{10}B^{2+}$ and $^{10}B^{1+}$ peaks in the mass spectrum. (For interpretation of the references to color in this figure legend, the reader is referred to the web version of this article.)

isotopic abundances may not reflect their true values, appropriate care must be exercised when using isotopic abundances for the deconvolution of overlapping peaks in the mass spectrum or for estimating the loss of signal due to dead-time effects. Furthermore, when possible, acquisition conditions should be chosen to minimize the number of multi-hit detection events.

In regards to the isotopic variations that were noted above for B, a quantum tunneling mechanism has been previously proposed and used to partially explain relative isotopic abundance variations that can occur within a given charge state for B [11,12,50]. However, the tunneling mechanism alone cannot explain the consistent under-representation of the major isotope that has been observed here for laser pulsed, i.e. thermally activated evaporation, of B and Si, or the loss of ^{10}B ion counts in monoisotopic ^{10}B implants. Detector dead-time effects are a possible explanation for these phenomena.

3.3. Ion correlation analysis

3.3.1. Two-dimensional ion correlation histograms

Ion correlation histograms comparing the (m/n) ratios of the first-of-multiples to the second-of multiples were plotted for the nominally pure B and SRM2137 specimen data acquired with the LEAP® 4000X-Si instrument using the same instrument parameters, Fig. 5(a) and (b).

Since each multi-hit event was recorded as a semi-transparent data point on the histogram, darker locations correspond to a greater number of points. A diagonal red reference line has been added along $y=x$, and corresponds to multi-hit events in which ion pairs of the same (m/n) ratio ions, such as $^{10}B^{+}/^{10}B^{+}$, impact the detector. Ions pairs in which both ions are the same isotope and have the same charge-state, i.e. same isotope, same charge-state (SISCS) ion pairs, are of specific interest in the discussion below.

The coincidence points between the major peaks of the mass spectrum are clearly visible for the two B isotopes, ^{10}B and ^{11}B, Fig. 5(a) and (b). Coincidence points are also present for the three Si isotopes, ^{28}Si, ^{29}Si, and ^{30}Si, (see also Fig. S3 in the Supplementary Materials online) in the SRM2137 specimen. The presence of residual hydrogen (H) was also evident in both histograms. The horizontal and vertical tracks emanating from the major peak coincidence points indicate that one of the ions in the multi-hit event was field evaporated concomitantly with the laser pulse, while the other ion was delayed in time. Additionally, the diagonal tracks that originate at the major peak coincidence points and extend to the upper-right indicate pairs of ions that field evaporate from the specimen surface together, but after a time delay relative to the laser pulse [48]. For the nominally pure B specimen, the two isotopes, ^{10}B and ^{11}B, are present at three different charge-states, 3+, 2+, and 1+. No evidence of ion dissociation reactions, complex ions, or molecular ions involving B was found in the correlation histograms or in the associated mass spectra. The SRM2137 specimen was implanted with ^{10}B, and so there is only faint evidence of the $^{11}B^{1+}$ in the ion correlation histogram. However, both the 2+ and 1+ charge-states are visible for the ^{10}B. There is also evidence of co-evaporation of H/B, B/Si, and H/Si ion pairs in the ion correlation histogram, but no complex ions containing these elements were observed. Nearly absent from the ion correlation histograms are the SISCS ion pairs, such as $^{10}B^{+}/^{10}B^{+}$, that fall on the $y=x$ reference line. Closer observation also reveals a depleted data zone immediately adjacent to the $y=x$ reference line.

3.3.2. Correlation of multi-hit events

The deficiency of multi-hit events along the $y=x$ reference line on the ion correlation histograms, Fig. 5(a) and (b), indicates that only a small number of SISCS ion pairs are detected as multi-hit events. Furthermore, diagonal, horizontal, and vertical tracks that represent the delayed evaporation of one or both ions in SISCS ion pairs are not present in the ion correlation histogram at the $y=x$ line. The lack of these features and the loss of signal in the data-depleted zone are due to the detector dead-time and the corresponding detector dead-zone.

As mentioned earlier, the ⁎.ePOS files can be filtered via a software algorithm to extract the ion information associated with a particular detection event multiplicity. For example, for multiplicity-2 events, the ion hit positions on the detector can be used to calculate the relative separation distance between the two ions in the pair [37,38]. The distribution of the separation distances at the detector between ions in multiplicity-2 events for the nominally pure B is illustrated in Fig. 6 and for the SRM2137 materials in Fig. 7. As discussed above, multi-hit events are closely correlated in space and time. For example, the majority of the ions pairs associated with multiplicity-2 events impacted the detector with a

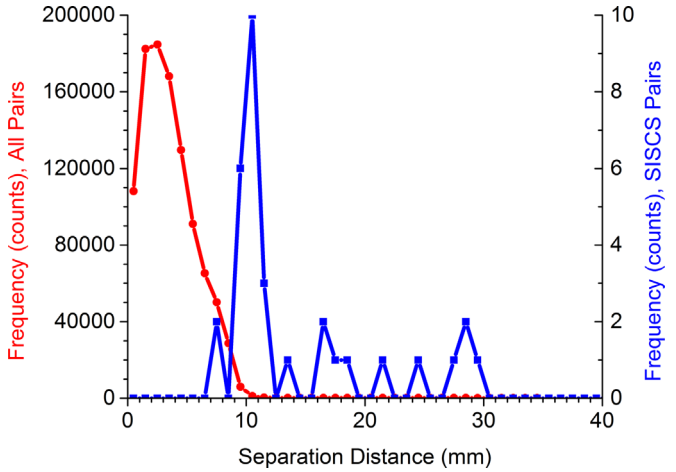

Fig. 6. Separation distance between ions in multiplicity-2 detection events of nominally pure B (20 pJ) for all ion pairs (red circles, median = 3.2 mm) and for SISCS ion pairs (blue squares, median = 10.8 mm). A larger median separation distance on the detector is required to resolve SISCS ion pairs. (For interpretation of the references to color in this figure legend, the reader is referred to the web version of this article.)

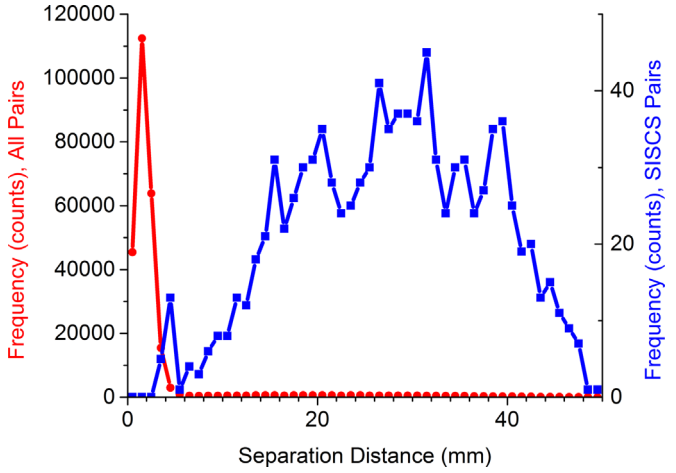

Fig. 7. Separation distance between ions in multiplicity-2 detection events of the SRM2137 (4000X-Si) specimen for all ion pairs (red circles, median = 1.75 mm) and for SISCS ion pairs (blue squares, median = 28.2 mm). (For interpretation of the references to color in this figure legend, the reader is referred to the web version of this article.)

median separation distance between ions of 3.2 mm for the nominally pure B specimens, Fig. 6, and 1.75 mm for the SRM2137 specimen (4000X-Si), Fig. 7. The exception to this behavior is, however, the SISCS ion pairs. The individual ions in these pairs attain equal velocity under the influence of the standing DC potential after field evaporation. These ions have the same flight times for equal flight path lengths, and therefore, in order for the detection system to resolve the individual ions of the SISCS ion pairs, the constituent ions must be separated by a minimum physical distance on the detector. If the separation distance is less than the minimum required value, the two ions in the pair will be detected as a single ion. Since most SISCS ion pair impacts are detected as a single ion, the true multiplicity of the detection events involving these ion pairings can be misclassified [16]. Furthermore, this implies that the number of isotopes and charge-states available under a given set of acquisition conditions may limit the maximum apparent multiplicity value that is observed. For example, a B data set with two isotopes at two charge-states provides four different (m/n) ratio ions that can be detected in different combinations. A true multiplicity-5 event, in this data set, would require at least one SISCS pair, thereby causing the event to be recorded with an apparent multiplicity of four or less due to the detector dead-time. For true multiplicity >1 events, the SISCS pairs formed from the major isotope will be the most abundant, with the result being that the signal loss will be greatest for the major isotope. Moreover, the multi-hit data will influence the multiplicity-1 (singles) mass spectrum by increasing the count for different isotopes in proportions that do not reflect the true isotope abundances. For the nominally pure B specimens, the median separation distance between ions in SISCS ion pair detection events (specified by a difference in (m/n) ratios <0.02) was 10.8 mm, Fig. 6. The minimum separation distances recorded were between 7 mm and 8 mm. Furthermore, very few of these ion pairs were detected as demonstrated by the frequency of hits relative to all multiplicity-2 event hits shown in Fig. 6. For the SRM2137 specimens, the median separation distance between ions in SISCS ion pairs was 28.2 mm, Fig. 7. The minimum separation distances recorded were between 3 mm and 4 mm. However, the frequency of the SISCS ion pair events decreases as the separation distance decreases below about 14 mm, Fig. 7, despite the fact that non-SISCS pairs overwhelmingly arrive with <6 mm of separation. Again, few of these SISCS ion pairs were detected when compared to the number of all ion pairs in the multiplicity-2 events.

Voltage pulsed data is also affected by the detector dead-time. As a result, the specimen composition determined by a voltage pulsed atom probe can vary significantly from the true value, as demonstrated by T. T. Tsong, et al. [17]. Further, Menand & Kingham have demonstrated that B can preferentially field evaporate in multi-hit events in voltage pulsed metallic glasses [11,12,50]. However, the nominally pure B specimens and the B-implanted Si specimens (SRM2137), which are semi-conducting materials, did not successfully run in voltage pulsed-mode. The effects of detector dead-time on voltage pulsed data are instead demonstrated with data acquired from a Si pre-sharp specimen. An ion correlation histogram and an ion separation distance histogram for voltage pulsed Si are provided in section S3.3.2 of the Supplementary Material. The Si data demonstrates that the dead-time affects voltage pulsed data in the same way that it effects laser pulsed data. For comparison, an additional ion correlation histogram for the laser pulsed SRM2137 (LEAP® 4000X-Si) specimen has also been included in the Supplementary Material (section S3.3.2).

3.4. Delayed field evaporation of ion pairs

The ion correlation histogram can provide insight into the field evaporation behavior of the ions in multi-hit detection events. When two ions having different (m/n) ratios concomitantly field evaporate from the specimen, but are delayed relative to the pulse, a slightly curved diagonal track is observed on the ion correlation histogram, Fig. 5(a) and (b). The track originates at the ion coincidence points corresponding to the major (m/n) peaks in the mass spectrum, but can accommodate a pair of ions field evaporating at any time between consecutive pulses, and time-wise, may even be counted with the subsequent pulse. The defining feature of the track is the constant difference in arrival time between the two ions in the pair [48]. The track therefore defines the apparent mass-to-charge ratios of the two ions, $(m/n)_1^{app}$, and $(m/n)_2^{app}$, as observed by the detector. Only one point on the track corresponds to the true mass-to-charge ratios, $(m/n)_1$ and $(m/n)_2$, of the ions in the pair – the origination point, as indicated in Fig. 5(a).

Given the expression for the (m/n) ratio of a detected ion, as derived from kinetic energy (KE) and potential energy (PE) considerations of the field evaporated ions [51], an analytical expression for the TOF difference between two ions in a multiplicity-2 event, Δt, can be derived,

$$\Delta t = \sqrt{\frac{(m/n)_2 d^2}{2eV}} - \sqrt{\frac{(m/n)_1 d^2}{2eV}} \quad (1)$$

where d is the flight distance, e is the charge of an electron, and V is the DC standing voltage applied between the specimen and the electrode. Similarly, the energy balance can be used to develop an analytical expression relating the apparent (m/n) ratios of the two ions in a multiplicity-2 ion pair to their true values. The ion correlation histograms presented thus far have been expressed in terms of (m/n) ratios of the first- and second-of-multiples. Therefore, it is desirable to express $(m/n)_2^{app}$ as a function of the other mass-to-charge ratios, $(m/n)_1^{app}$, $(m/n)_1$, and $(m/n)_2$, so that the resulting analytical Eq. (2) can be plotted directly onto the ion correlation histogram for comparison with the experimental data. For a fully detailed derivation of Eq. (2), the reader is referred to section S3.4 of the Supplementary Material.

$$\left(\frac{m}{n}\right)_2^{app} = \left(\frac{m}{n}\right)_1^{app} + 2\sqrt{\left(\frac{m}{n}\right)_1^{app}\left(\frac{m}{n}\right)_2} - 2\sqrt{\left(\frac{m}{n}\right)_1^{app}\left(\frac{m}{n}\right)_1} + \left(\frac{m}{n}\right)_2 - 2\sqrt{\left(\frac{m}{n}\right)_1\left(\frac{m}{n}\right)_2} + \left(\frac{m}{n}\right)_1 \quad (2)$$

Eq. (2) is plotted on the arsenic-implanted Si ion correlation histogram in Fig. 8 for two empirical tracks (dotted red curves). The validity of Eq. (2) can be further checked by testing it at $(m/n)_1^{app} = (m/n)_1$ and noting that it correctly yields $(m/n)_2^{app} = (m/n)_2$, which are the coordinates of the origination point of the track. When the actual (m/n) ratios are equal, $(m/n)_1 = (m/n)_2$, expression (2) yields $(m/n)_2^{app} = (m/n)_1^{app}$, which is the $y=x$ reference line discussed above, upon which the coincidence points of SISCS ion pairs lie. Again, because of detector dead-time effects, the ion information along this line is sparse. The pronounced delayed evaporation tracks that are observed in Fig. 5(a) and (b) for the other ion pairs associated with the major peaks in the mass spectrum, are absent for the SISCS ion pairs along the y=x line. While Eq. (2) is non-linear on (m/n) ratio ion correlation histograms, the constant difference in arrival time between $(m/n)_1$ and $(m/n)_2$ means the diagonal track will be linear on an ion correlation histogram plotted in terms of corrected TOF (see Fig. S4 in the Supplementary Material).

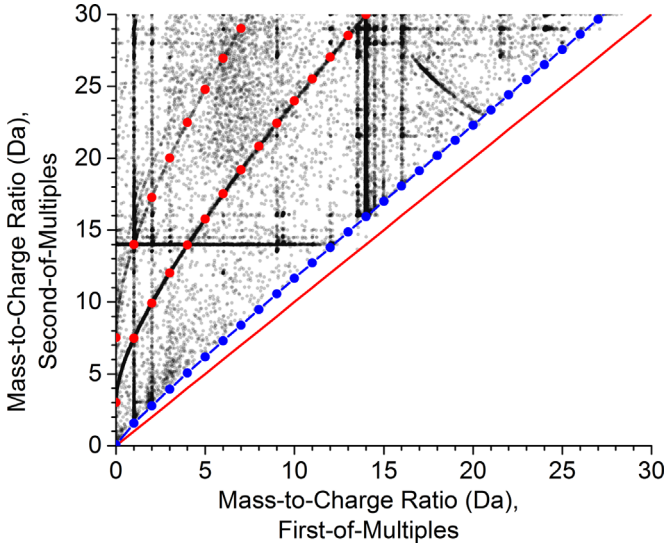

Fig. 8. Mass-to-charge ratio ion correlation histogram for arsenic implanted Si (3000X-Si). The red dotted curves show the derived analytical solution (Eq. (2)) as applied to two empirical tracks on the histogram. The blue line with circle markers is the same analytical expression used to delineate the data depleted zone representing a dead-time of about 18 ns above the $y=x$ reference line. (For interpretation of the references to color in this figure legend, the reader is referred to the web version of this article.)

3.5. Estimating detector dead-time and observing the detector dead-zone

Since the effect of dead-time is an important signal loss mechanism, three approaches for estimating the detector dead-time were evaluated and checked for consistency between one another. One method for determining the detector dead-time is to measure it directly from the ion correlation histogram generated from the multiplicity-2 detection events. If the ion correlation histogram is plotted using the corrected TOF values for the ion pairs, the width of the depleted data zone along the $y=x$ line is a direct measure of the dead-time (see Fig. S4 in the Supplementary Material). Alternatively, if the ion correlation histogram is plotted using (m/n) ratios, then Eq. (1) can be used to determine the TOF difference between the two ions in a pair that lie on the depleted data zone boundary. This TOF difference will be an estimate of the detector dead-time. For the full details on the ion correlation histogram based methods used, the reader is referred to section S3.5 in the Supplementary Material. Both of the aforementioned ion correlation histogram based methods yielded a dead-time of approximately 3 ns for the LEAP® 4000X-Si.

A third method to estimate the detector dead-time is to use an algorithm to read and filter the ⁎.ePOS data in order to extract specific multi-hit ions according to the TOF difference between the individual ions in each pair [35]. By first filtering out ion pairs with long TOF differences between them and extracting only the ion pairs that have a short TOF difference between them, SISCS ion pairs will be selected almost exclusively. A frequency histogram of the detector separation distances between the ions in these pairs will show a large median separation distance between the individual ions. As the filter cut-off value is increased to admit ion pairs having increasingly large TOF differences, the median separation distance between the ions will diminish, as demonstrated in Fig. 9. The dead-time will be the TOF difference that eliminates the most ion pairs with short separation distances. For the nominally pure B data set (20 pJ) acquired in the 4000X-Si configuration instrument, a TOF difference of about 3.25 ns eliminated all

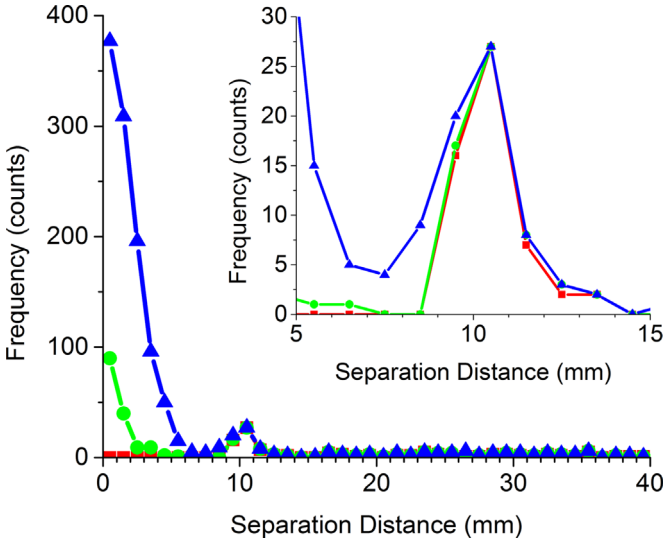

Fig. 9. Frequency distributions for the detector separation distance between the individual ions of multiplicity-2 pairs of nominally pure B (20 pJ). The ions have been filtered to remove ions pairs with TOF differences greater than 3 ns (red squares), greater than 4 ns (green circles), and greater than 5 ns (blue triangles). The median separation distance between the ions increases as the TOF difference between the ions decreases. Below the detector dead-time of about 3 ns, ions will be resolved when the separation distance exceeds the dead-zone size. (For interpretation of the references to color in this figure legend, the reader is referred to the web version of this article.)

ion pairs from the multiplicity-2 events with a separation distance of less than 9 mm on the detector, thereby validating the ion correlation histogram based methods for determining the dead-time. The apparent peak near 10 mm separation distance, in Fig. 9, is likely the right-most tail of the true SISCS ion pair separation distance distribution. The majority of the true SISCS ion pair distribution having been lost and not recorded due to the effects of the detector dead-time. For the arsenic-implanted Si data set acquired in the 3000X-Si configuration instrument, the cut-off was abrupt, with no multiplicity-2 ion pairs found for time-of flight differences below 20 ns, which is within the known dead-time range for this instrument. With regard to Fig. 9, for dead-times up to 6 ns, ion pairs continue to be added to the 0–2 mm separation distance bins. The ions in these bins are very close together in space and time, even relative to the other multiplicity-2 pairs. Beyond 6 ns, few, if any, counts are added to the 0-2 mm bins. This suggests that the loss of data as a result of the dead-time effects is not confined only to the 3.25 ns estimate that was determined earlier, but rather a partial loss of ion pair data extends to about 6 ns for the 4000X-Si configuration instrument. A partial loss of ion pairs having a TOF difference of up to 6 ns would, for example, be comparable to the difference in (m/n) ratio between $^{28}Si^{2+}$ and $^{29}Si^{2+}$ at 5000 V. Furthermore, since the TOF difference between the two ions in a given pair decreases as the standing DC voltage increases, it will become more difficult to resolve the individual ions in the pair as the acquisition voltage increases and the TOF difference between the two ions becomes small relative to the dead-time. For example, at an acquisition voltage of 6000 V (90 mm flight path), the TOF difference between $^{206}Pb^{1+}$ and $^{207}Pb^{1+}$ is about 3 ns, whereas the TOF difference between $^{10}B^{1+}$ and $^{11}B^{1+}$ is about 13 ns. Similarly, at an acquisition voltage of 2000 V (90 mm flight path), the TOF difference between $^{206}Pb^{3+}$ and $^{207}Pb^{3+}$ is about 3 ns, whereas the TOF difference between $^{10}B^{3+}$ and $^{11}B^{3+}$ is about 13 ns. Thus, as the acquisition voltage increases, the ability to resolve different isotopes in the multi-hit data will be lost first at higher atomic numbers and/or higher charge states.

As discussed earlier, the ions in SISCS pairs have the same flight times for equal flight path lengths. In order for the detection system to resolve the individual ions of the SISCS ion pairs, the constituent ions must be separated by a minimum physical distance on the detector, which defines a dead-zone around the first hit. A custom algorithm was used to read the ∗.ePOS data and extract only the multiplicity-2 ion pairs with TOF differences less than the detector dead-time of 3.25 ns. By plotting the relative position of the second hit with respect to the first hit, the detector dead zone can be mapped, Fig. 10. The orientations of the three DLD anode wires lying horizontally, vertically, and at 45° are clearly visible as regions of depleted data in Fig. 10.

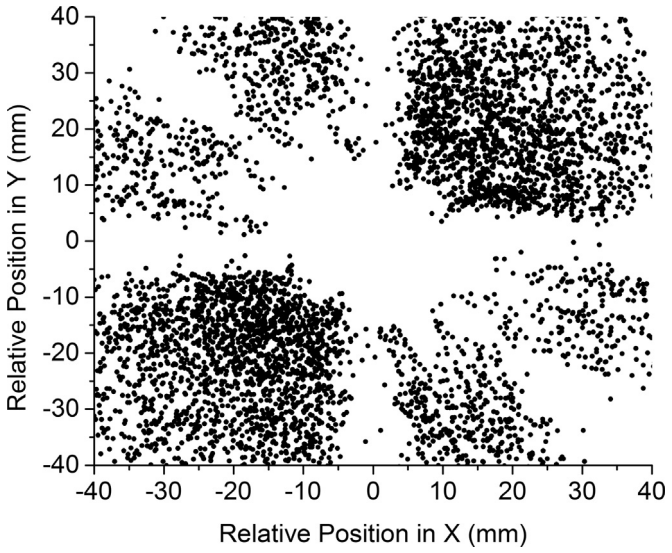

Fig. 10. Detector dead-zone plot as indicated by multiplicity-2 events having constituent ions separated by a TOF difference of less than 3.25 ns. The orientations of the three DLD anode wires in the LEAP® 4000X-Si instrument are clearly visible in the plot.

3.6. The signal in multi-hit detection events

3.6.1. The fraction of the boron signal contained in multi-hit events

The fraction of the B signal that was detected in the multi-hit data is determined from the ranged mass spectra, Fig. 2(a) and (b) and Fig. 3. For the two nominally pure B specimens, the ratio of the number of B ions detected in multi-hit events to the total number of B ions detected in all detection events was approximately 0.7 using background corrected integrated peak intensities. This ratio was approximately 0.6 for the nominally pure B when only the peak maxima were used. In the SRM2137 specimens, a similar detection ratio of approximately 0.8 was determined for the ^{10}B signals in the LEAP® 4000X-Si configuration instrument using integrated peak intensities and a detection ratio of approximately 0.7 was determined using the peak maxima only. For the LEAP® 4000X-HR configuration instrument, a detection ratio of approximately 0.6 was determined using the integrated peak intensities, and a ratio of 0.6 was calculated from peak maxima only. Thus, the B is preferentially detected in multi-hit events whether it is found in high or minor-to-trace concentrations. This is consistent with the findings of Menand, et al., who had demonstrated that B preferentially field evaporates in multi-hit events in response to thermally activated evaporation [11,12,50]. Additionally, in the B-doped Si materials, the different evaporation fields of B and Si may contribute to the observed phenomenon. Boron reportedly has a high evaporation field of 64 V nm^{-1}, while that of Si is 33 V nm^{-1}[52]. If B is preferentially retained on the surface of the SRM2137 specimen, then the surface concentration would increase with time until the field was high enough to field evaporate the B atoms [10,53], which may then lead to the formation of multiples. However, while preferential surface retention may be able to explain the behavior of B in Si, the same mechanism cannot explain the field evaporation behavior in nominally pure B where equally high fractions of the B signal were found in the multi-hit data.

The multiplicity frequency distributions [37] for both the nominally pure B specimens and the SRM2137 specimens are presented in Fig. 11. Multiplicity-2 events are the most commonly recorded multi-hit detection event. The number of events detected decreases with increasing multiplicity and no events having a multiplicity greater than five were detected in the course of this study, for either type of specimen. For the nominally pure B specimens, less than 40% of the total detection events were multi-hit events, however, $>60\%$ of the ranged B ions were found within multi-hit events. For the SRM2137 material, less than 3% of the total detection events were multi-hit, yet $>60\%$ of the B signal was contained within multi-hit events, similar to the nominally pure B specimens. This is quite remarkable, considering the wide concentration range spanned by these two materials and may hint at the possibility of determining a correction factor that can be employed across this concentration range to provide accurate quantitative analyses of B [54].

It is important to remember, however, that the true multiplicity of any given detection event is uncertain. Given that constituent SISCS ion pairs within a given high multiplicity event will likely be recorded as a single ion impact, the true multiplicity of the event may be higher than the apparent value that was recorded by the

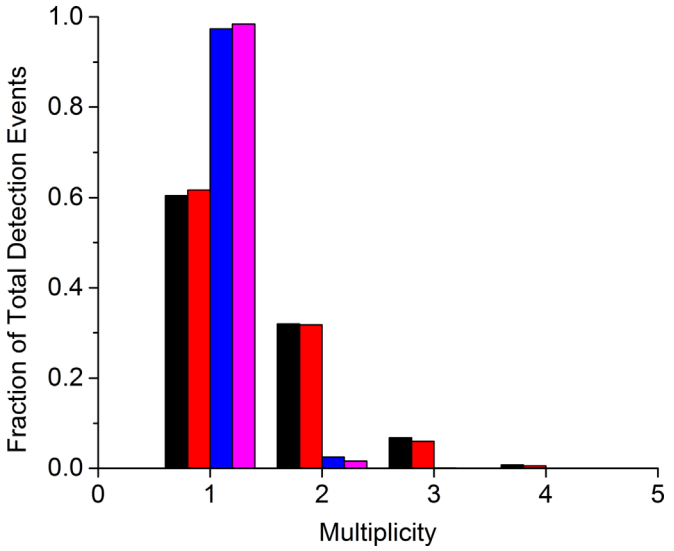

Fig. 11. Multiplicity frequency distributions for (left to right): B at 30 pJ (black), B at 20 pJ, (red), SRM2137 from LEAP® 4000X-Si instrument (blue), and SRM2137 from LEAP® 4000X-HR instrument (pink). (For interpretation of the references to color in this figure legend, the reader is referred to the web version of this article.)

detection system. For example, many SISCS true multiplicity-2 events are recorded as single (or multiplicity-1) events. Likewise, a true multiplicity-3 event consisting of $^{10}B^{1+}$,$^{10}B^{1+}$, and $^{11}B^{1+}$ may be recorded as a multiplicity-2 event.

Given the above discussion, nominally pure B appears to be an excellent specimen material for testing the response of an atom probe ion detection system to multi-hit events. Not only is B preferentially detected in multi-hit detection events, but the mass spectrum for nominally pure B is simple, and shows no evidence for the formation of complex or molecular ions that contain B. Furthermore, the mass spectrum for B provides information on two different isotopes at multiple charge-states, which allows for the measurement and critical evaluation of isotopic abundances.

3.6.2. Estimating the magnitude of the boron signal loss

A number of different probability-based correction schemes have been proposed in an effort to estimate the signal loss that results from ion pile-up [16–18,36,55]. Given the simplicity of the mass spectrum for nominally pure B, a first-order approximation was made of the fraction of the B signal that is lost through dead-time related effects. The probability of recording a particular mix of isotopes in a multiplicity-2 event was determined from a multinomial distribution, as was the probability of recording a particular mix of charge states in a multiplicity-2 event. The presence of multiple charge-states must be accounted for, since it increases the probability of detecting ion pairs of the same isotope, e.g. $^{10}B^{1+}/^{10}B^{2+}$. Additional details regarding the assumptions and procedures used to calculate the signal loss estimate are provided in the online Supplementary Material (section S3.6.2). For the two nominally pure B specimens, the fraction of signal loss was estimated at about 0.2, with only the 2+ and 1+ charge states active. The expression derived for signal loss indicates that the loss should be minimized when the acquisition conditions are such that the two charge-states occur with equal probability.

The above discussion on estimating the B signal loss provides some insight into how an APT experiment might be designed to reduce the ion signal loss that results from the effects of the detector dead-time and is equally applicable to both laser pulsing and voltage pulsing. Since it is the SISCS ion pairs that are significantly affected by this loss mechanism, acquisition conditions that create an increased opportunity for the formation of non-SISCS ion pairs could serve to reduce the observed signal loss - e.g. analyses that have a larger number of elements, isotopes, and/or charge states in the mass spectrum. Generally, the specimen composition cannot be chosen to optimize the APT analysis, so it is through control of the charge state distribution that ion signal loss may be ameliorated.

4. Conclusions

The impact of the detector dead-time on the quantitative analysis of nominally pure boron (B), Si, and for B-implanted Si (NIST-SRM2137) with a retained ^{10}B dose of about 1×10^{15} atoms cm^{-2} was investigated. Ion correlation analyses were used to graphically demonstrate the impact of detector dead-time on multi-hit detection events. Given the important role of detector dead-time as a signal loss mechanism, three different methods for estimating the detector dead-time were presented. The following findings resulted from this research:

1. Boron can be significantly under-measured in atom probe analyses. The B signal losses observed in this study were estimated at 20–36% of the total B signal.
2. The detector dead-time is a significant signal loss mechanism for multi-hit detection events, and thus for B. The detector dead-time results in few same isotope same charge state (SISCS) ion pairs being recorded by the atom probe detector, with the major isotopes suffering the greatest ion signal losses. Additionally, a region of depleted data can be observed in the ion correlation histogram. The boundary of this depleted data zone can be described by an analytical solution that was derived to model the delayed co-evaporation tracks in the ion correlation histogram.
3. The dead-time for the CAMECA LEAP® 4000X-Si atom probe instrument was estimated to be about 3 ns, with a partial loss of data extending to about 6 ns. Furthermore, it was demonstrated that this detector dead-time can be used to plot the dead-zone that surrounds a first-of-multiples ion detection event.
4. The median separation distance between constituent ions in multiplicity-2 events was measured. For the SRM2137 (LEAP® 4000X-Si) specimen, the median separation distance was 1.75 mm for all ion pairs and 28.2 mm for the SISCS ion pairs. For nominally pure B (20 pJ) the median separation distance was 3.2 mm for all ion pairs and 10.8 mm for the SISCS ion pairs.

Acknowledgments

The authors would like to thank Dr. David J. Larson, Dr. Ed Oltman, Dr. Robert M. Ulfig, Dr. Hugues Francois Saint-Cyr, and Dan Lawrence of CAMECA, Inc. for providing details of the arsenic-implanted Si specimen, for assisting with specimen coating processes, and for many helpful discussions throughout this study. The authors are also grateful for the specimen materials provided by Dr. Doug Meier and Dr. Albert Davydov of the NIST and for the dual-beam FIB/SEM instrument access that was granted by Dr. Babak Nikoobakht and Dr. Keana Scott of the NIST. One author, R. Prakash Kolli, would also like to extend his gratitude to Professor Sreeramamurthy (Rama) Ankem of the University of Maryland – College Park.

Appendix A. Supplementary material

Supplementary data associated with this article can be found in the online version at http://dx.doi.org/10.1016/j.ultramic.2015.07.009.

References

[1] P. Cogez, M. Graef, B. Huizing, R. Mahnkopf, H. Ishiuchi, J. Shindo et al., The International Technology Roadmap for Semiconductors, 2011 Edition Metrology, International Roadmap Committee, 2011.

[2] P. Cogez, M. Graef, B. Huizing, R. Mahnkopf, H. Ishiuchi, J. Shindo et al., The International Technology Roadmap for Semiconductors, 2012 Update, International Roadmap Committee, 2012.

[3] E. Cadel, F. Vurpillot, R. Larde, S. Duguay, B. Deconihout, Depth resolution function of the laser assisted tomographic atom probe in the investigation of semiconductors, J. Appl. Phys. 106 (2009) 044908-1–044908-6.

[4] L.J. Lauhon, P. Adusumilli, P. Ronsheim, P.L. Flaitz, D. Lawrence, Atom-probe tomography of semiconductor materials and device structures, MRS Bull. 34 (2009) 738–743.

[5] D.J. Larson, T.J. Prosa, D. Lawrence, B.P. Geiser, C.M. Jones, T.F. Kelly, Atom probe tomography for microelectronics, Handb. Instrum. Tech. Semicond. Nanostruc. Charact., 2011, pp. 407–470.

[6] B. Gault, M.P. Moody, J.M. Cairney, S.P. Ringer, Experimental Setup, in: At. Probe Microsc., Springer: New York, 2012, pp. 43–47.

[7] K. Thompson, D. Lawrence, D.J. Larson, J.D. Olson, T.F. Kelly, B. Gorman, In situ site-specific specimen preparation for atom probe tomography, Ultramicroscopy. 107 (2007) 131–139, http://dx.doi.org/10.1016/j.ultramic.2006.06.008.

[8] T.J. Prosa, D. Olson, B. Geiser, D.J. Larson, K. Henry, E. Steel, Analysis of implanted silicon dopant profiles, Ultramicroscopy. 132 (2013) 179–185, http://dx.doi.org/10.1016/j.ultramic.2012.10.005.

[9] P. Ronsheim, P. Flaitz, M. Hatzistergos, C. Molella, K. Thompson, R. Alvis, Impurity measurements in silicon with D-SIMS and atom probe tomography, Appl. Surf. Sci. 255 (2008) 1547–1550, http://dx.doi.org/10.1016/j.apsusc.2008.05.247.

[10] G.D. Costa, H. Wang, S. Duguay, A. Bostel, D. Blavette, B. Deconihout, Advance in multi-hit detection and quantization in atom probe tomography, Rev. Sci. Instrum. 83 (2012) 123709, http://dx.doi.org/10.1063/1.4770120.

[11] A. Menand, D.R. Kingham, Evidence for the quantum tunnelling of boron ions, J. Phys. C: Solid State Phys. 18 (1985) 4539–4547.

[12] A. Menand, C. Martin, J. Sarrau, Field evaporation charge state of boron ions: a temperature effect study, J. Phys. Colloq. 45 (1984), C9–95–C9–98.

[13] E.A. Marquis, J.M. Hyde, Applications of atom-probe tomography to the characterisation of solute behaviours, Mater. Sci. Eng.: R: Rep. 69 (2010) 37–62, http://dx.doi.org/10.1016/j.mser.2010.05.001.

[14] T. Kinno, H. Akutsu, M. Tomita, S. Kawanaka, T. Sonehara, A. Hokazono, et al., Influence of multi-hit capability on quantitative measurement of NiPtSi thin film with laser-assisted atom probe tomography, Appl. Surf. Sci. 259 (2012) 726–730, http://dx.doi.org/10.1016/j.apsusc.2012.07.108.

[15] L. Yao, B. Gault, J.M. Cairney, S.P. Ringer, On the multiplicity of field evaporation events in atom probe: a new dimension to the analysis of mass spectra, Philos. Mag. Lett. 90 (2010) 121–129, http://dx.doi.org/10.1080/09500830903472997.

[16] A. Cerezo, G. Smith, A. Waugh, The FIM100-performance of a commercial atom probe system, J. Phys. Colloq. 45 (1984) 329–335.

[17] T.T. Tsong, Y.S. Ng, S.V. Krishnaswamy, Quantification of atom-probe FIM data and an application to the investigation of surface segregation of alloys, Appl. Phys. Lett. 32 (1978) 778–780.

[18] U. Rolander, H.O. Andren, Statistical correction for pile-up in the atom-probe detector system, J. Phys. Colloq. 50 (1989) 529–534.

[19] S. Boninelli, S. Mirabella, E. Bruno, F. Priolo, F. Cristiano, A. Claverie, et al., Evolution of boron-interstitial clusters in crystalline Si studied by transmission electron microscopy, Appl. Phys. Lett. 91 (2007) 031905, http://dx.doi.org/10.1063/1.2757145.

[20] W. Luo, P. Clancy, Identification of stable boron clusters in c-Si using tight-binding statics, J. Appl. Phys. 89 (2001) 1596, http://dx.doi.org/10.1063/1.1335644.

[21] F. Tang, B. Gault, S.P. Ringer, J.M. Cairney, Optimization of pulsed laser atom probe (PLAP) for the analysis of nanocomposite Ti–Si–N films, Ultramicroscopy. 110 (2010) 836–843, http://dx.doi.org/10.1016/j.ultramic.2010.03.003.

[22] F. De Geuser, B. Gault, A. Bostel, F. Vurpillot, Correlated field evaporation as seen by atom probe tomography, Surf. Sci. 601 (2007) 536–543, http://dx.doi.org/10.1016/j.susc.2006.10.019.

[23] M. Gruber, F. Vurpillot, A. Bostel, B. Deconihout, Field evaporation: a kinetic monte carlo approach on the influence of temperature, Surf. Sci. 605 (2011) 2025–2031.

[24] Thomas F. Kelly, T.T. Gribb, D. Olson, L. Martens, J.D. Shepard, S.A. Wiener, et al., First data from a commercial local electrode atom probe (LEAP), Microsc. Microanal. 10 (2004) 373–383.

[25] A. Cerezo, T.J. Godfrey, G.D.W. Smith, Application of a position-sensitive detector to atom probe microanalysis, Rev. Sci. Instrum. 59 (1988) 862–866.

[26] D. Blavette, B. Deconihout, A. Bostel, J.M. Sarrau, M. Bouet, A. Menand, The tomographic atom probe: a quantitative three-dimensional nanoanalytical instrument on an atomic scale, Rev. Sci. Instrum. 64 (1993) 2911–2919.

[27] D. Blavette, J.M. Sarrau, A. Bostel, J. Gallot, Direction et distance d'analyse a' la sonde atomique, Rev. Phys. Appl. 17 (1982) 435–440.

[28] P. Bas, A. Bostel, B. Deconihout, D. Blavette, A general protocol for the reconstruction of 3D atom probe data, Appl. Surf. Sci. 87-88 (1995) 298–304.

[29] B.P. Geiser, D.J. Larson, E. Oltman, S. Gerstl, D. Reinhard, T.F. Kelly, et al., Wide-field-of-view atom probe reconstruction, Microsc. Microanal. 15 (2009) 292–293.

[30] F. Vurpillot, B. Gault, B.P. Geiser, D.J. Larson, Reconstructing atom probe data: a review, Ultramicroscopy. 132 (2013) 19–30.

[31] J.V. Vallerga, J.B. McPhate, Optimization of the readout electronics for microchannel plate delay line anodes, in: Int. Symp. Opt. Sci. Technol., International Society for Optics and Photonics, 2000: pp. 34–42. ⟨http://proceedings.spiedigitallibrary.org/proceeding.aspx?articleid=919916⟩ (accessed 13.03.14).

[32] O. Jagutzki, V. Mergel, K. Ullmann-Pfleger, L. Spielberger, U. Spillmann, R. Dörner, et al., A broad-application microchannel-plate detector system for advanced particle or photon detection tasks: large area imaging, precise multi-hit timing information and high detection rate, Nucl. Instrum. Methods Phys. Res. Sect. A: Accel. Spectrom. Detect. Assoc. Equip. 477 (2002) 244–249.

[33] I. Ali, R. Dörner, O. Jagutzki, S. Nüttgens, V. Mergel, L. Spielberger, et al., Multi-hit detector system for complete momentum balance in spectroscopy in molecular fragmentation processes, Nucl. Instrum. Methods Phys. Res. Sect. B: Beam Interact. Mater. At. 149 (1999) 490–500.

[34] O. Jagutzki, A. Cerezo, A. Czasch, R. Dorner, M. Hattas, Min Huang, et al., Multiple hit readout of a microchannel plate detector with a three-layer delay-line anode, IEEE Trans. Nucl. Sci. 49 (2002) 2477–2483, http://dx.doi.org/10.1109/TNS.2002.803889.

[35] U. Rolander, H.O. Andren, Study of proper conditions for quantitative atom-probe analysis, Appl. Surf. Sci. 76/77 (1994) 392–402.

[36] A. Menand, T. Al Kassab, S. Chambreland, J. Sarrau, Atom-probe study of aluminum–lithium alloys, J. Phys. Colloq. 49 (C6) (1988), C6–353–C6–358.

[37] M. Müller, D.W. Saxey, G.D.W. Smith, B. Gault, Some aspects of the field evaporation behaviour of GaSb, Ultramicroscopy. 111 (2011) 487–492.

[38] M. Thuvander, A. Kvist, L.J.S. Johnson, J. Weidow, H.-O. Andrén, Reduction of multiple hits in atom probe tomography, Ultramicroscopy. 132 (2013) 81–85, http://dx.doi.org/10.1016/j.ultramic.2012.12.005.

[39] National Institute of Standards and Technology Certificate of Analysis, 2010.

[40] D.S. Simons, R.G. Downing, G.P. Lamaze, R.M. Lindstrom, et al., Development of certified reference materials of ion-implanted dopants in silicon for calibration of secondary ion mass spectrometers, J. Vac. Sci. Technol. B 25 (2007) 1365–1375.

[41] M.K. Miller, K.F. Russell, G.B. Thompson, Strategies for fabricating atom probe specimens with a dual beam FIB, Ultramicroscopy. 102 (2005) 287–298, http://dx.doi.org/10.1016/j.ultramic.2004.10.011.

[42] R.P. Kolli, F. Meisenkothen, A focused ion beam specimen preparation method to minimize gallium ion concentration in Copper Atom-Probe Tomography Specimen Tips, Microsc. Microanal. 20 (S3) (2014) 350–351, http://dx.doi.org/10.1017/S143192761400347X.

[43] K. Thompson, B. Gorman, D.J. Larson, B. van Leer, L. Hong, Minimization of Ga induced FIB damage using low energy clean-up, Microsc. Microanal. 12 (2006) 1736–1737.

[44] A. Cerezo, G.D.W. Smith, P.H. Clifton, Measurement of temperature rises in the femtosecond laser pulsed three-dimensional atom probe, Appl. Phys. Lett. 88 (2006) 154103, http://dx.doi.org/10.1063/1.2191412.

[45] D.J. Larson, T.J. Prosa, R.M. Ulfig, B.P. Geiser, T.F. Kelly, Data processing and reconstruction, in: Local Electrode At. Probe Tomogr., Springer, 2013, pp. 109–162. http://link.springer.com/chapter/10.1007/978-1-4614-8721-0_5 (accessed 26.03.14).

[46] D.J. Larson T.J. Prosa R.M. Ulfig B.P. Geiser Kelly F. Thomas Appendix A: data file formats, in: Local Electrode At. Probe Tomogr. Users Guide, Springer, New York, 2013, pp. 249–256.

[47] B. Gault, M.P. Moody, J.M. Cairney, S.P. Ringer, Appendix: File Formats Used in APT, in: At. Probe Microsc., Springer, New York, 2012, pp. 322–329.

[48] D.W. Saxey, Correlated ion analysis and the interpretation of atom probe mass spectra, Ultramicroscopy. 111 (2011) 473–479, http://dx.doi.org/10.1016/j.ultramic.2010.11.021.

[49] R.P. Kolli, F. Meisenkothen, The influence of experimental parameters and specimen geometry on the mass spectra of copper during pulsed-laser atom-probe tomography, Microsc. Microanal. 20 (2014) 1715–1726, http://dx.doi.org/10.1017/S1431927614013488.

[50] A. Menand, D.R. Kingham, Isotopic variations in field evaporation charge-state of boron ions, J Phys Appl Phys. 17 (1984) 203–208.

[51] E.W. Müller, J.A. Panitz, S.B. McLane, The atom-probe field ion microscope, Rev. Sci. Instrum. 39 (1963) 83–86.

[52] T.T. Tsong, Field ion image formation, Surf. Sci. 78 (1978) 211–233.

[53] M.K. Miller, Preferential Retention and Evaporation, in: At. Probe Tomogr. Anal. At. Level, Kluwer Academic/Plenum Publishers, New York, 2000, pp. 127–129.

[54] D.J. Larson, Atom probe tomography: technology and Semiconductor Applications, 26th Annual Workshop on Secondary Ion Mass Spectrometry, National Harbor, MD, May 27 - May 30, 2014.

[55] T. Stephan, P.R. Heck, D. Isheim, J.B. Lewis, Correction of dead time effects in laser-induced desorption time-of-flight mass spectrometry: applications in atom probe tomography, Int. J. Mass Spectrom. (2015) 1–6.

[56] F. Meisenkothen, T.J. Prosa, E.B. Steel, R.P. Kolli, The role of multi-hit detection events on the accurate measurement of boron in atom probe tomography, Microsc. Microanal. 20 (S3) (2014) 1962–1963, http://dx.doi.org/10.1017/S1431927614011544.